Applied Surface Science 622 (2023) 156913

Contents lists available at ScienceDirect

Applied Surface Science

journal homepage: www.elsevier.com/locate/apsusc

Full Length Article

The complex heterogeneous Fenton reactivity of transition metal-doped ferrihydrite: Insight from the structural variation and pathway of H_2O_2 activation

Qingru Xie [a,b], Yanping Zhu [a,c,*], Haiyang Xian [a,b], Qingze Chen [a,b], Chengshuai Liu [b,d], Fei Wu [b,d], Xiaoliang Liang [a,b], Runliang Zhu [a,b,*]

[a] CAS Key Laboratory of Mineralogy and Metallogeny/Guangdong Provincial Key Laboratory of Mineral Physics and Materials, Guangzhou Institute of Geochemistry, Chinese Academy of Sciences (CAS), Guangzhou 510640, China
[b] University of Chinese Academy of Sciences, Beijing 100049, China
[c] Guangdong Provincial Key Laboratory of Agricultural & Rural Pollution Abatement and Environmental Safety, College of Natural Resources and Environment, South China Agricultural University, Guangzhou 510642, China
[d] State Key Laboratory of Environmental Geochemistry, Institute of Geochemistry, Chinese Academy of Sciences, Guiyang 550081, China

ARTICLE INFO

Keywords:
Transition metal-doped ferrihydrite
Heterogeneous Fenton reaction
H_2O_2 activation
Oxygen vacancies
Reactive oxygen species

ABSTRACT

Doping transition metal into ferrihydrite (Fh) may significantly affect its structure and Fenton reactivity. The comparative study of Fh and M(II)-Fh (M = Cu, Co, or Mn), for the first time, reveals that doping metal ions can alter the property and content of oxygen vacancy (OVs) and the oxidation potential of Fh, which subsequently affects H_2O_2 decomposition, $HO^{\cdot}$ generation, and Fenton reactivity of the catalysts. The overall Fenton activity of the samples in decomposing bisphenol A decreases in the order Cu-Fh > Fh > Co-Fh > Mn-Fh. In specific, Cu-Fh is the most efficient catalyst as it has the lowest energy barrier for decomposing H_2O_2 into $HO^{\cdot}$ at OVs sites and the highest oxidation potential (benefiting the reduction of Fe(III) to Fe(II) by H_2O_2). Our findings show the complex heterogeneous Fenton reactivity of M-Fh, and doping can be an efficient strategy for achieving highly efficient Fenton catalysts.

1. Introduction

Iron (oxyhydr)oxides, as important natural heterogeneous Fenton catalysts, are ubiquitous on the earth's near-surface and can activate H_2O_2 to generate highly reactive $HO^{\cdot}$ (Eqs. (1) and (2)) [1–4]. This process is vital for the self-cleaning of environment (using natural H_2O_2) and for the degradation of organic contaminants during the remediation of polluted soils (using intentionally added H_2O_2) [5,6]. Besides, iron (oxyhydr)oxides are important precursors/components for synthesizing highly efficient heterogeneous Fenton catalysts [7–11].

$$\equiv Fe(III) + H_2O_2 \rightarrow \equiv Fe(II) + HO_2^{\cdot} + H^+,\ K = 0.01\ M^{-1}s^{-1} \quad (1)$$

$$\equiv Fe(II) + H_2O_2 \rightarrow \equiv Fe(III) + HO^{\cdot} + OH^-,\ K = 40\text{–}80\ M^{-1}s^{-1} \quad (2)$$

Among the various iron (oxyhydr)oxides, the poorly crystalline ferrihydrite (Fh) has drawn particular concerns as heterogeneous Fenton catalyst [12–14]. Fh has a much high redox potential (~0.2 mV) than most other iron (oxyhydr)oxides (generally varying between -300 and -200 mV) [15], rendering Fh a better oxidizing capacity (i.e., electron-accepting capacity); in other words, the rate-limiting step for reducing Fe(III) to Fe(II) (Eqs. (1)) can be accomplished more easily by Fh. Besides, with a nano-sized particle (2–6 nm) and large specific surface area (~300 m^2/g) [16,17], Fh can provide abundant active sites for Fenton reaction, and also be an ideal support/component for synthesizing novel heterogeneous Fenton catalysts. For example, recent studies from our group combined various functional materials (e.g., $BiVO_4$, Ag/AgCl, or carbon nanotube) with Fh, and the resulting composites showed highly efficient Fenton catalytic activity [12–14].

Naturally occurring Fh always contains substitution ions (Al, Co, Cu, Mn, Si, etc.) in the structure, because of the complexity of the supergene environment [18–20]. These impurity ions can change the composition, microstructure, surface properties, and crystallinity of Fh, thereby affecting its activity [21–25]. For example, Ni et al. (2016) reported that the Al-doped Fh showed a higher pH_{pzc} value and a larger specific

* Corresponding authors.
E-mail addresses: zhuyanping@scau.edu.cn (Y. Zhu), zhurl@gig.ac.cn (R. Zhu).

https://doi.org/10.1016/j.apsusc.2023.156913
Received 8 November 2022; Received in revised form 24 February 2023; Accepted 28 February 2023
Available online 5 March 2023

surface area compared with Fh, which is favorable for the adsorption of Cr(VI). Several studies demonstrated that the doping of metal ions (e.g., Ni, Co, Cu, Zn, or Al) can retard the transformation of Fh to goethite/hematite [21,23]. However, the effects of doping ions on the heterogeneous Fenton activity of Fh have been overlooked, and a large knowledge gap remains in this area.

Besides, doping is also a common strategy for improving the activity of many functional materials [26–31], and several studies indeed have investigated the Fenton catalytic activity of some metal-doped iron (oxyhydr)oxides (e.g., magnetite, goethite, and hematite) [9,32–34]. Theoretically, doping transition metals into iron (oxyhydr)oxides may change their structure, and thus have multiple effects on their Fenton catalytic activity: (1) Generating new oxygen vacancies (OVs) on the catalysts. Although OVs is the ubiquitous defects in the structure of iron (oxyhydr)oxides, doping metal ions can always create new OVs (i.e., $OVs_{(M\text{-}Fe)}$), particularly when the doped metal ions have a different valence than the original one [35,36]. As OVs possess localized electrons that can promote the heterolytic H_2O_2 dissociation to generate $HO^{\cdot}$ [37], these newly formed $OVs_{(M\text{-}Fe)}$ may have additional complex effects on the Fenton catalytic activity of doped Fh. (2) Changing the electronic structure. The potentials corresponding to the bottom of conduction band (CB) and top of valence band (VB) is the oxidation potential and reduction potential of catalyst, respectively [38,39]. The doped metal can modify the reducing/oxidizing capacity of the catalyst by changing the edge positions of CB and VB [40], which may further affect their capacity of accepting electrons from H_2O_2 to reduce Fe(III) during the Fenton reaction process. Therefore, doping metal ions into Fh might be able to change its structure and thus the catalytic performance as well, which remain to be clarified.

According to the above discussion, studying the structure and Fenton reactivity of M-Fh has at least the following multiple meanings: (1) M-Fh are ubiquitous in the nature and will participate in the degradation of natural organic contaminants through Fenton reaction; the related study will help understand the important role of M-Fh in self-cleaning of environment and soil remediation. (2) Doping transition metal into Fh may be a feasible and facile strategy for promoting its Fenton activity, and the related study will help design efficient heterogeneous Fenton catalysts. (3) Doping is a convenient method for dictating Fh's structure and activity, and a detailed study of how the specific structural feature (e.g., $OVs_{(M\text{-}Fe)}$) of M-Fh affects their Fenton activity will help clarify the complex mechanisms of heterogeneous Fenton reaction system.

In this term, we select Cu(II), Mn(II), and Co(II) as doping ions to illustrate the effect of doped transition metals on the structure and heterogeneous Fenton activity of Fh. The morphology and structure of these M-Fh were characterized using TEM, XRD, XPS, EPR, and low-temperature Mössbauer spectra. Density functional theory (DFT) simulations were applied to determine the detailed reaction process for generating $HO^{\cdot}$ on the $OV_{(Fe\text{-}Fe)\ or\ (M\text{-}Fe)}$. Furthermore, batch experiments such as the decomposition of H_2O_2, the generation of $HO^{\cdot}$, O_2, and Fe(II), and the degradation of organic contaminants were conducted to verify the possible decomposition pathway of H_2O_2 induced by M-Fh.

2. Materials and methods

2.1. Chemicals

$Fe(NO_3)_3{\cdot}9H_2O$, $Cu(NO_3)_2{\cdot}6H_2O$, $Co(NO_3)_2{\cdot}6H_2O$, $Mn(NO_3)_2$ (50 wt %), Na_2SO_4, HNO_3, H_2O_2 (30 wt%), NaOH, benzoic acid (BA), *p*-benzoquinone (BQ), bisphenol A (BPA), isopropanol (IPA), *p*-hydroxybenzoic acid (*p*-HBA) were obtained from Aladdin Industrial Corporation (Shanghai, China). 5,5-Dimethyl-1-pyrroline-*N*-oxide (DMPO) was obtained from Sinopharm Chemical Reagent Co. ltd., China. CH_3COOH, CH_3COONH_4, and 1,10-phenanthroline monohydrate were purchased from the Guangzhou Chemical Reagent Factory (Guangzhou, China). All reagents were of analytical grade and used as received.

2.2. Synthesis of Fh, Cu-Fh, Co-Fh, and Mn-Fh

The synthesis of two-line Fh was based on the protocol of Cismasu et al (2012). In detail, 40 mL of $Fe(NO_3)_3{\cdot}9H_2O$ (1 M) and 20 mL of NaOH (6 M) were simultaneously titrated to pH 7 ± 0.1 under continuous magnetic stirring for 2 h. Then, all precipitates were centrifuged and washed with ultrapure water four times. M-Fh (Cu-Fh, Co-Fh, and Mn-Fh) was synthesized as described above with the addition of the nitrate salts of Cu, Co, or Mn, and the desired M/(M + Fe) molar percentages were controlled at 1 mol% and 5 mol% M. In addition, Co-Fh, and Mn-Fh were synthesized under N_2 atmosphere to avoid oxidation by air.

2.3. Characterization

Rigaku MiniFlex-600 X-ray diffractometer (Cu Kα radiation) over the 2θ range of 3-80° at 3°/min was employed to obtain X-ray powder diffraction (XRD) patterns. X-ray photoelectron spectroscopy (XPS) patterns were recorded on a Thermo Fisher Scientific K-Alpha spectrometer equipped with Al Kα source. The C1s peak (284.80 eV) of the adventitious carbon-based contaminant was used as a reference for calibration. Transmission electron microscopy (TEM) images with selected-area electron diffraction (SAED) patterns and energy diffraction spectrum (EDS) were performed with an FEI Talos F200S instrument equipped with an acceleration voltage of 200 kV. Mössbauer spectra were collected using the standard Mössbauer instrumentation by WissEl GmbH (Starnberg) with a source of 57Co in the Rh (14.4 keV gamma rays) matrix at a temperature of 12 K. The Moss Winn computer program was used to evaluate all raw spectra. The flat band potential (E_{fb}) of Fh and 5 %M-Fh was measured by Mott-Schottky analysis, and the Mott-Schottky analysis was carried out at 2 kHz frequency (the working electrode is Fh or 5 %M-Fh; the counter-electrode is a Pt sheet; the reference electrode is an Ag/AgCl (saturated KCl) electrode).

2.4. Heterogeneous Fenton catalytic experiments

The heterogeneous Fenton experiments of BPA degradation were performed in a 50 mL conical flask containing 50 mg catalyst and 10 mg/L BPA solution (pH value was adjusted at 3). The conical flask with catalyst and BPA solution was constantly stirred for 30 min to ensure the adsorption–desorption equilibrium before dropping 0.5 mL H_2O_2 (1 M) into the conical flask. During the reaction, a 0.8 mL sample solution was collected and filtered with a Millipore filter (pore size of 0.22 μm) at each time interval for analysis.

The high pressure liquid chromatography (HPLC, 1260, Agilent) with a Luna 5μ C18 column (250 mm) was used to quantify the concentration of BPA. The settings for the HPLC measurement were as follows: the mobile phase is comprised of water and acetonitrile (50:50, v/v) at the wavelength of 230 nm. UV-vis spectroscopy (759S, Shanghai Jing Hua Instrument Co. ltd.,) was used to calculate the concentration of H_2O_2 (Xu et al., 2017). In addition, the generated O_2 was collected using a commercially available automatic testing system (Labsolar-6A, Perfectlight), and the content was detected by gas chromatography (GC7900, Techcomp Group).

Spectrophotometric determination of Fe(II) with 1,10-phenanthroline monohydrate combined with the Chinese national standard method of GB/T 6730.71–2014 was used to measure the generation of Fe(II) on the samples [41,42]. Specifically, HCl (1 mL, 6 M), Na_2CO_3 (0.2 g) were added into the collected precipitation (after centrifugation) to dissolve the samples entirely, and the produced CO_2 by Na_2CO_3 can help prevent Fe(II) oxidation [12,13,42]. After that, the NH_4F (1 mL, 10 M) CH_3COONH_4-CH_3COOH buffer solution (pH 4.2, 1 mL), and 1,10-phenanthroline monohydrate (1 mL, 0.5 % (m/v)) were introduced into the above reaction system, which then result in the formation of a complex [13]. UV–vis spectroscopy was used to quantify the concentration of the complex at 510 nm.

2.5. Analysis of reactive oxygen species and oxygen vacancies

The generated HO· was measured using BA as a probe molecule [12–14], and the experimental operations for capturing free radicals were unanimous as those in the heterogeneous Fenton catalysis experiment. In brief, the oxidation of BA (10 mM) to *p*-HBA is a probe reaction for reflecting the generation of HO· in the heterogeneous Fenton catalysis reaction, and the calculation of cumulative HO· concentration is referred to Eq. 3 [12,13,33]. The Agilent 1260 HPLC was used to measure the concentration of *p*-HBA, and the settings for the measurement were as follows: mobile phase, acetonitrile, and 0.1 % TFA aqueous solution (35:65, v/v); analysis wavelength, 255 nm. IPA (5 mM) as the scavenge of HO· was added to the system, and then the degradation of BPA was monitored. The experimental operations for capturing free radicals were unanimous as those in the heterogeneous Fenton catalysis experiments.

$$\text{Cumulative } [HO\cdot] \text{ produced} = [p\text{-HBA}] \times 5.87. \quad (3)$$

The low-temperature EPR spectra (JES FA200, JEOL) was conducted to determine the presence of OVs on the samples, and the EPR spectra (JES-FA200, JEOL) were used to analyze the formation of O_2^-. The modulation frequency for the EPR spectrum of O_2^- was 100 kHz.

2.6. DFT calculation

All DFT calculations within the generalized-gradient approximation

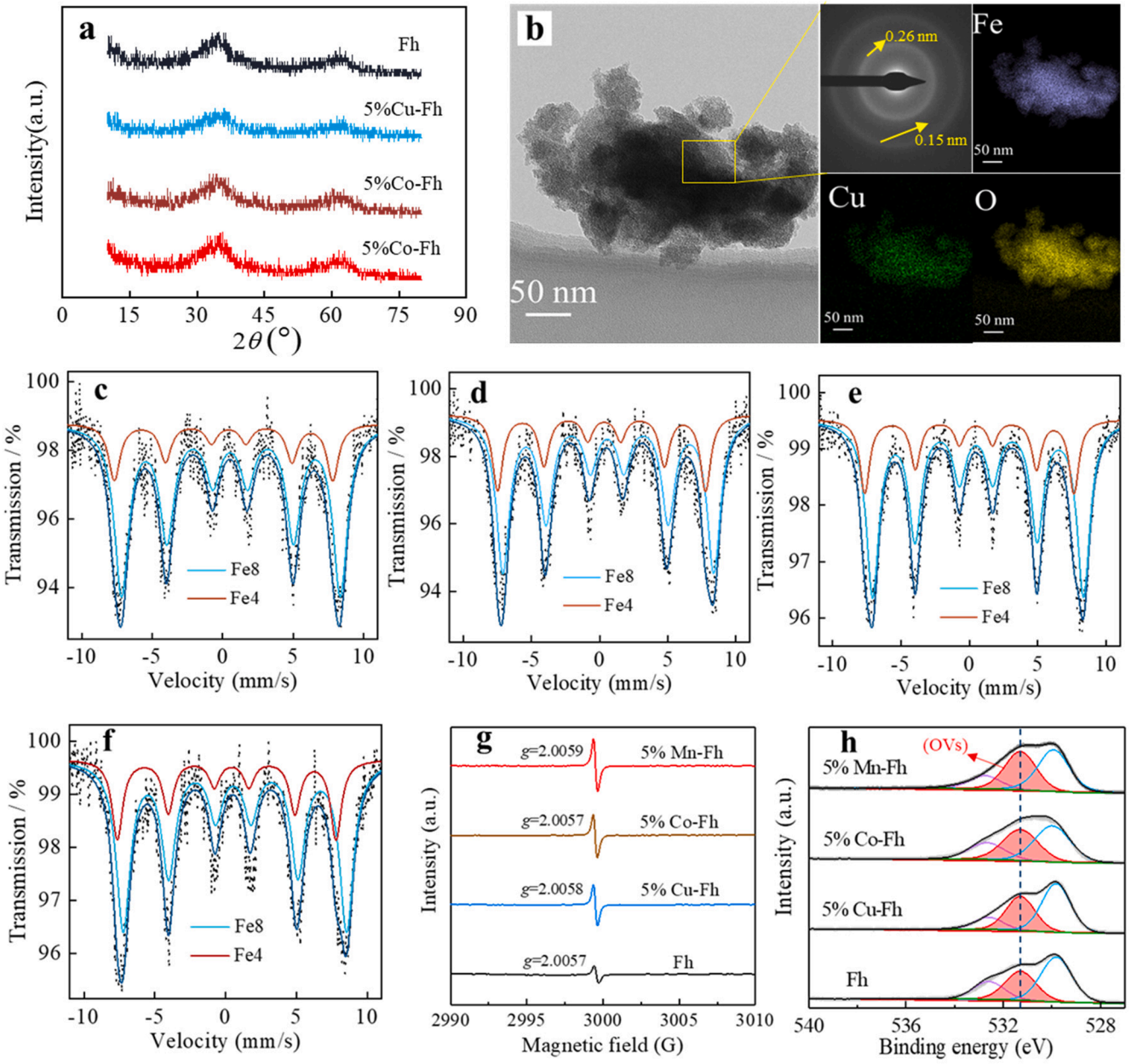

Fig. 1. (a) XRD patterns of Fh and 5 %M-Fh (M = Cu, Co, and Mn); (b) TEM image of 5 %Cu-Fh, and the corresponding EDS mapping images and selected area electron diffraction pattern. The yellow arrows in the selected area of the electron diffraction patterns indicate diffraction rings for different 5 %M-Fh, with the corresponding *d*-spacing of ~ 0.15 and ~ 0.26 nm; Mössbauer spectra of (c) Fh, (d) 5 %Cu-Fh, (e) 5 %Mn-Fh, and (f) 5 %Co-Fh measured at the temperature of 12 K. The iron positions of Fh and 5 %M-Fh correspond to tetrahedrally (Fe4) and octahedrally (Fe8) coordinated iron. The relative area of the Fe4 site is decreased after doping with Cu, Co, and Mn; (g) the low-temperature EPR spectra of oxygen vacancies (OVs) in Fh and different 5 %M-Fh; (h) the O 1 s XPS spectra of Fh and different 5 %M-Fh. (For interpretation of the references to colour in this figure legend, the reader is referred to the web version of this article.)

(GGA) were performed using the Vienna *ab initio* Simulation Package (VASP5.4.4) along with the projector augmented wave (PAW) method [43]. The energy cutoff was set to 600 eV for a 10^{-6} eV/cell convergence of the total energy. The energy and force convergence thresholds at which all atoms are released during the structure optimization iteration are set to be 10^{-4} eV and 0.03 eV/ Å. The cluster model of Fh with unit cell-size ($Fe_{10}O_{16}H_2$) was used as the optimized conventional cell [17], and then the optimized cell of $1 \times 2 \times 2$ is carved out of an extended bulk crystal cleaved along the stable (1 1 0) crystallographic planes [44], as shown in Fig. S2a. Based on the former supercell, the M-Fh model with an OV was simulated by substituting a 4-fold coordinated Fe atom on the Fh(0 0 1) surface with an M (i.e., Cu, Co, or Mn) atom according to the results of Mössbauer spectra, XPS, and EPR characterization (see below), and then removing an oxygen atom which links to the 6-fold coordinated Fe atom and the M atom, as shown in Fig. 2a. A ($3 \times 3 \times 1$) K-point grid is used for structural optimization and electronic structural calculations, and DFT-D3 method is adopted to accurately describe the van der Waals force interaction between catalysts and adsorbates. Moreover, the vacuum layer thickness of 20 Å is set in the z-direction. In addition, the energies of an OV formation (E_{vac} (f)) is defined by the formula of E_{vac} (f) = $E_{vac} + E\frac{1}{2}O_2 - E_{st}$, where E_{vac}, $E\frac{1}{2}O_2$, and E_{st} is the energy of a supercell with an OV, the half energy of an O_2 molecule in the gas phase, the energy of a supercell without an OV, respectively [45,46]. The E_{ad} (i.e., the adsorption energy) can be obtained by the formula of $E_{ad} = E_{sa} - (E_{cs} + E_{as})$, where E_{sa}, E_{cs}, and E_{as} is the total energy of substrate with adsorbates, the total energy of the clean substrate, and the total energy of insulated adsorption species, respectively. The charge density difference was calculated as $\Delta\rho = \rho_{A+B} - \rho_A - \rho_B$, where ρ_X is the electron charge density of X. Furthermore, the Löwdin population analysis has been used to compare the degree of charge transfer quantitatively [47].

3. Results and discussion

3.1. Structural characteristics of the samples

The XRD patterns of Fh, 5 %M-Fh and 1 %M-Fh (M = Cu, Co, and Mn) are presented (Fig. 1a and Fig. S1a). All samples exhibit a signal of two broad reflections at approximated-spacings of ~ 0.15 and ~ 0.26 nm, confirming the presence of 2-line Fh [17]. The presence of Co, Cu, or Mn does not cause evident differences in the XRD reflections, which should be attributed to the weak crystalline structure of Fh, showing apparent peak broadening [18,19]. The doping of metal ions will be further investigated using the low-temperature Mössbauer spectra in subsequent work.

The morphological details and the element distribution of 5 %Cu-Fh (Fig. 1b), 5 %Co-Fh, and 5 %Mn-Fh (Fig. S1b-c) were collected by TEM and EDX mapping. The EDS mapping of the selected samples shows that O, Fe, Cu, Mn, and Co elements are homogeneously distributed, indicating the uniform dispersion of doping elements. In addition, the electron diffraction patterns of the selected area for different 5 %M-Fh show the diffraction rings corresponding to the d-spacing of ~ 0.15 and ~ 0.26 nm for Fh, well consistent with above XRD results.

The Mössbauer spectra were carried out at a temperature of 12 K to

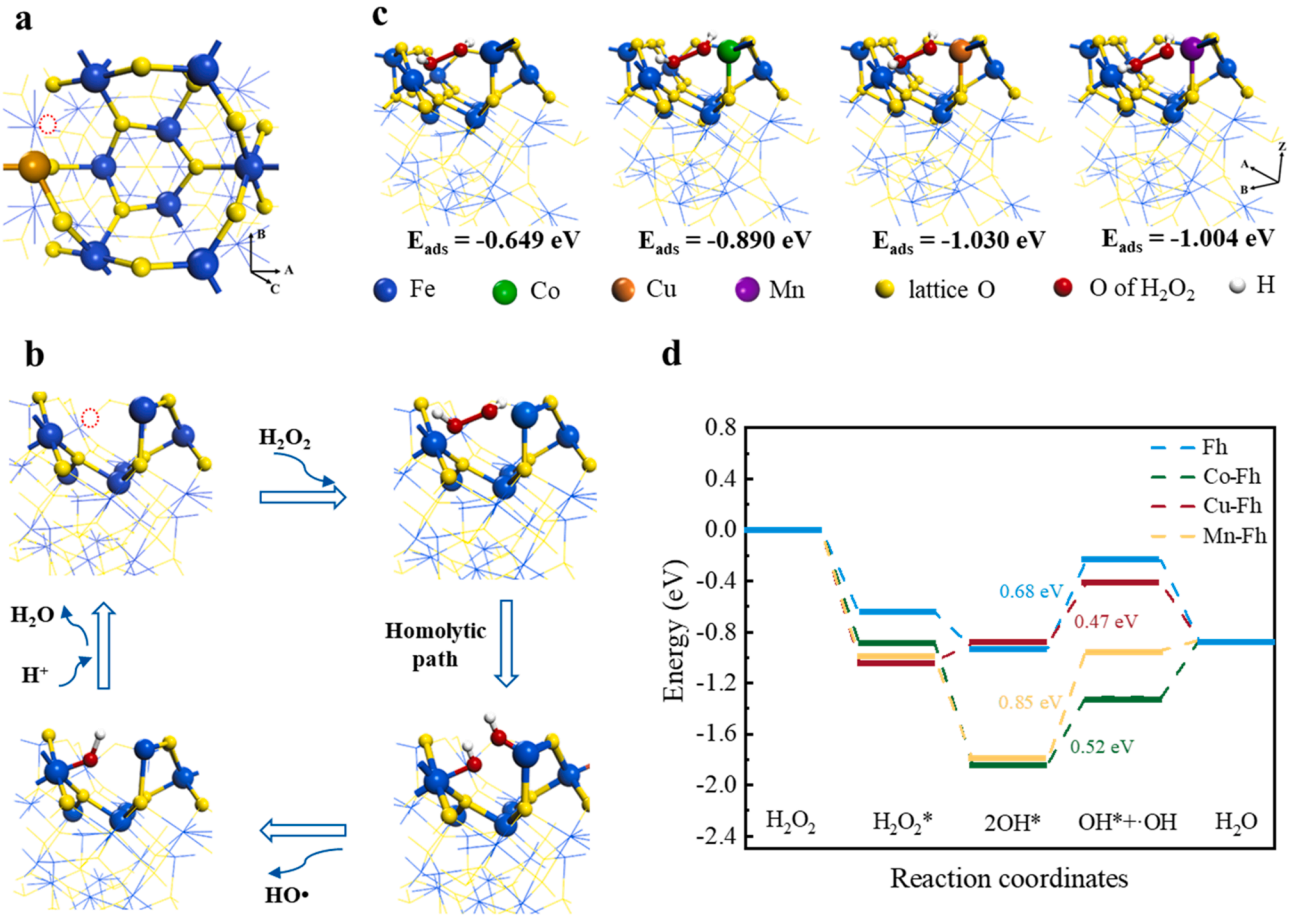

Fig. 2. (a) The most stable relaxed configurations of M-Fh (0 0 1) surfaces with an OV (the red dotted line circle), and the brown sphere represents the M atom (M = Cu, Co, or Mn); (b) the proposed reaction process of H_2O_2 activation into HO· at the Fe-Fe dual catalytic sites on the Fh surface; (c) adsorption of H_2O_2 on the Fh and M-Fh (0 0 1) surface with an OV; (d) energy diagram of the proposed reaction process for Fh and M-Fh models. (For interpretation of the references to colour in this figure legend, the reader is referred to the web version of this article.)

probe the occupied sites of doping cations (Fig. 1c-f). The Mössbauer spectra of both Fh and M-Fh show two overlapping sextet hyperfine patterns, which correspond to ^{57}Fe in tetrahedral (Fe4) and octahedral (Fe8) sites, respectively. The isomer shift (IS) is consistent with values reported in other studies and shows the range for Fe4 of 0.23–0.42 mm s^{-1} and Fe8 of 0.35–0.59 mm s^{-1} [48-50]. The relative area of the Fe4 site is decreased after doping with Co, Mn, or Cu (Fig. 1c-f and Table 1), suggesting that the doped cations are mainly replacing the tetrahedral Fe^{3+} in Fh. In particular, the change in the relative area of the Fe4 site caused by Mn doping is more significant than those caused by Co or Cu doping, which should be attributed to the similar ionic radius of Mn^{2+} vs Fe^{3+} (67 and 65 pm respectively) [51], resulting in an easier structural substitution of Mn^{2+} for Fe^{3+} in Fh.

The existence of crystal defects (e.g., OVs) in the Fh structure is evident. More OVs will be created to maintain the electrostatic balance because the doped metal has lower valence than Fe(III) in the Fh structure [35,36]. The energies of an OV formation (E_{vac} (f)) on the Fh and M-Fh surfaces have been listed in Table 2 and follow the order: Fh (-7.44 eV) > Co-Fh (-7.52 eV) > Cu-Fh (-7.77 eV) > Mn-Fh (-8.21 eV). The formation of OVs will be more favorable in the M-Fh surfaces than in the Fh surface from a thermodynamic aspect, and there may be more OVs on the surface of M-Fh than on the surface of Fh. As such, XPS analysis and EPR spectra were used to identify the existence of OVs in Fh, 5 %Cu-Fh, 5 %Co-Fh, and 5 %Mn-Fh (Fig. 1g-h). The EPR signal at g = 2.005 can be ascribed to OVs, and the intensity of EPR signal increases with the increment of OVs amount [52,37]. According to the intensity, the amount of the OVs decreases in the order: 5 %Mn-Fh > 5 %Co-Fh > 5 %Cu-Fh > Fh (Fig. 1g). In the XPS analysis (Fig. 1h), the O1s spectra of Fh, 5 %Cu-Fh, 5 %Co-Fh, and 5 %Mn-Fh are deconvoluted into three distinct peaks corresponding to oxygen atoms of diverse states: lattice oxygen species at 529.3–530.5 eV, the adsorbed oxygen OVs at 530.5–531.7 eV, and adsorbed H_2O at 531.8–533.2 eV [52,53]. The relative OVs concentration can be approximated by dividing the area of the OVs peak to the area of the whole O 1 s. The relative OVs concentration is 31 %, 37 %, 38 %, and 41 %, respectively, in Fh, 5 %Cu-Fh, 5 % Co-Fh, and 5 %Mn-Fh, which follows the same trend as detected by EPR characterization. It seems that the OVs amounts in M-Fh are closely related to the ionic radius of the doped metal: a similar ionic radius will result in easier substitution, and subsequently will create more OVs amounts to keep the electrostatic balance. As a result, Mn (67 pm) doped Fh has more OVs amounts than the Co (75 pm) or Cu (73 pm) doped Fh. These discrepancies may regulate the surface activity of Fh, which will be discussed later.

3.2. The activation of H_2O_2 by OVs

After identifying the doping sites and the existence of OVs in Fh and M-Fh, we constructed the models of Fh with an OV (Fig. S2b) and M-Fh with an OV (Fig. 2a) for DFT calculation. When the lattice oxygen atom leaves the oxide to form an OV, the electrons associated with the removed oxygen atom (i.e., $2e^-$) will redistribute to the surrounding metal cations (i.e., the localized electrons) [35,36]. The abundant localized electrons around OVs can improve the adsorption and activation of various molecules [37]. For example, an OV provides unsaturated coordination sites to attract H_2O_2 and the H_2O_2 can chemically bond to the metal atoms around the OV. Then, the localized electrons are transferred from the metal cations around the OV to adsorbed H_2O_2 (i.e., the consumption of localized electrons on the metal atoms and the accumulation of electrons on the O—O of H_2O_2), which facilitates the heterolytic dissociation of H_2O_2 to generate a OH^- bound on the metal atom and a free $HO^\cdot$ [37,53]. In addition, the new OVs created by the doped metal ions (i.e., $OVs_{(-Fe)}$) may have different behaviors in adsorbing and activating H_2O_2. As such, we calculated the process involving the activation of H_2O_2 and generation of $HO^\cdot$ at $OV_{(Fe-Fe)}$ or $OV_{(-Fe)}$ (i.e., $OV + H_2O_2 \rightarrow HO^\cdot + OH^-$).

The detailed reaction processes for generating $HO^\cdot$ on the $OV_{(Fe-Fe)}$ were proposed (Fig. 2b): (1) H_2O_2 is first adsorbed on $OV_{(Fe-Fe)}$ and then chemically bond to a 3-fold coordinated Fe atom and a 5-fold coordinated Fe atom in a side-on bridging mode [36,53]; (2) the bond H_2O_2 is homogeneously dissociated to form two hydroxyl groups at the 3-fold coordinated Fe site and the 5-fold coordinated Fe site, respectively [53,54]; (3) one hydroxyl group desorbs from the 3-fold coordinated Fe site to generate a reactive hydroxyl radical [36] (DFT results showed that the desorption of the hydroxyl group from the 5-fold coordinated Fe site makes the model unstable, and therefore we only need to consider the desorption of the hydroxyl group from the 3-fold coordinated Fe site for the following reaction paths); (4) the other adsorbed hydroxyl group reacts with a proton under acidic conditions to generate H_2O and then desorbed form the catalyst surface [36,55]. The reaction energy in above reaction processes was calculated accordingly (Fig. 2). Based on the obtained adsorption energy (Fig. 2c), the adsorption energy of H_2O_2 on the $OV_{(Fe-Fe)}$, $OV_{(Co-Fe)}$, $OV_{(Cu-Fe)}$, and $OV_{(Mn-Fe)}$ is -0.65, -0.89, -1.03, and -1.00 eV, respectively, following the trend of Cu-Fh > Mn-Fh > Co-Fh > Fh. Thus, the adsorption of H_2O_2 was more favorable at $OV_{(M-Fe)}$ than at $OV_{(Fe-Fe)}$, and the $OV_{(Cu-Fe)}$ shows the highest capacity for adsorbing H_2O_2. Besides, the desorption of hydroxyl group from the 3-fold coordinated Fe/M site to form a reactive hydroxyl radical is the rate-determining step (RDS) in the reaction process for generating $HO^\cdot$ [47]. According to the energy diagram (Fig. 2d), the energy barrier of RDS in different systems follows an order of Mn-Fh (0.85 eV) > Fh (0.68 eV) > Co-Fh (0.52 eV) > Cu-Fh (0.47 eV), which displays that $OV_{(Cu-Fe)}$ and $OV_{(Co-Fe)}$ exhibit higher H_2O_2 activation capacity than $OV_{(Fe-Fe)}$, while the capacity of generation of $HO^\cdot$ at $OV_{(Mn-Fe)}$ is lower. The charge transfer for generating $HO^\cdot$ was shown in Table 2. The two adsorbed hydroxyl groups accept electrons of -0.35 $|e|$, -0.31 $|e|$, -0.32 $|e|$, and -0.37 $|e|$ from the metal site in the Fh, Cu-Fh, Co-Fh, and Mn-Fh, respectively. As a result, the Cu-Fh and Co-Fh have less charge transfer between the adsorbed hydroxyl groups and the metal site than Fh, which indicates that the hydroxyl group dissociates easier from the metal site for the Cu-Fh and Co-Fh to form $HO^\cdot$ than Fh. The above theoretical results suggest that Cu-Fh might be the most promising candidate for H_2O_2 activation, owing to its highest capacity in adsorbing H_2O_2 and lowest energy barrier for generating $HO^\cdot$.

Table 1
Low-temperature Mössbauer parameters for Fh and 5%M-Fh. IS is the chemical isomer shift, QS is the quadrupole splitting, H is the hyperfine field, and A is the area under the partial doublet (occupancy of the position).

Sample	Position	IS (mm s^{-1})	QS (mm s^{-1})	H (T)	A (%)
Fh	Fe4	0.12	-0.38	47.29	27.48
	Fe8	0.59	0.08	47.96	72.52
5 %Co-Fh	Fe4	0.24	-0.34	47.87	26.58
	Fe8	0.59	0.11	48.89	73.42
5 %Cu-Fh	Fe4	0.24	-0.48	47.41	24.35
	Fe8	0.56	0.14	47.79	75.65
5 %Mn-Fh	Fe4	0.24	-0.37	48.06	20.98
	Fe8	0.55	0.05	48.12	79.02

Table 2
Comparison of Fh and M-Fh. The contents of the comparison are listed below: 1) the ionic radius of Fe^{3+} vs M^{2+}; 2) the concentration of OVs; 3) the formation energy of a single OV in Fh or M-Fh; 4) the adsorption energy of H_2O_2 on the OV; 5) the energy barrier of RDS on the OV; 6) The charge transfer between the adsorbed hydroxyl groups and the metal site.

	Fh	Cu-Fh	Co-Fh	Mn-Fh
Radius of Fe^{3+} or M^{2+} / pm	65	73	75	67
OVs concentration / %	31	37	38	41
E_{vac} (f) /eV	-7.44	-7.77	-7.52	-8.21
Adsorption energy of H_2O_2 / eV	-0.65	-1.03	-0.89	-1.00
Energy barrier of RDS / eV	0.68	0.47	0.52	0.85
Δq / $\|e\|$	-0.35	-0.31	-0.32	-0.37

3.3. Influence of the doped metal on the oxidation potential of Fh

The doped metal ions may modify the oxidizing potential of catalysts [40], which could further affect their capacity of accepting electrons from H_2O_2 to generate Fe(II) during the Fenton reaction process. In addition, the kinetics of Eqs. (1) is several orders of magnitude slower than that of Eqs. (2), and therefore the oxidizing capacity of the catalyst (i.e., the generation of Fe(II)) is critical to Fenton catalysis process [55,56]. In this term, the Mott-Schottky plots were measured to verify the oxidation potential of Fh and 5 %M-Fh. According to the Mott-Schottky plots (Fig. 3a), the slope of all samples is positive, as expected for an *n*-type semiconductor, indicating that the E_{fb} is nearly equal to the CB potential [12]. The determined E_{fb} values of Fh, 5 %Cu-Fh, 5 %Co-Fh, and 5 %Mn-Fh are about -0.54, -0.47, -0.52, and -0.54 V vs *SEC*, respectively. Thus, the CB potential is estimated to be -0.30, -0.23, -0.28, and -0.30 V vs NHE. When the catalyst is an electron acceptor, the potential corresponding to the bottom of CB is the oxidation potential [39]. Above results reveal that the oxidation potential of Fh, 5 %Co-Fh, and 5 %Mn-Fh are indeed comparable while the oxidizing capability of 5 %Cu-Fh slightly increased, suggesting that Fe(III) on 5 % Cu-Fh should be more easily reduced by H_2O_2 to generate Fe(II) (Eq. (1)).

Indeed, we directly detected the Fe(II) content on Fh and M-Fh, which follows the trend of 5 %Cu-Fh > Fh ≈ 5 %Co-Fh ≈ 5 %Mn-Fh (Fig. 3b), well in accordance with their oxidation potential (Fig. 3a). These results, from different aspects, indicate that Cu-Fh should be more efficient Fenton catalyst than other samples.

3.4. Detection of H_2O_2 activation

The concentrations of HO· were directly measured to verify the activation of H_2O_2 to HO· by Fh or M-Fh (Fig. 3c). After 120 min's reaction, the concentration of HO· in different systems follows the order: 5 %Cu-Fh (137.1 μmol/L) > 5 %Co-Fh (68.2 μmol/L) > Fh (56.8 μmol/L) > 5 %Mn-Fh (33.1 μmol/L). The generation of HO· in the Fh system was 18.7 μmol/L within 60 min, comparable with the vaules from previous studies (i.e., 15.1 or 15.6 μmol/L) that applied Fh as heterogeneous Fenton catalysts to generate HO· [14,57]. In addition, the concentration of HO· in 5 %Cu-Fh and 5 %Co-Fh systems is about 2.4 times and 1.2 times higher than that in the pure Fh system, respectively. Conversely, the concentration of HO· in the 5 %Mn-Fh system is much smaller than those in the Fh system. Therefore, 5 %Cu-Fh is the most promising candidate for HO· generation.

According to above analysis (i.e., parts 3.2 and 3.3), the different concentration of HO· in the Fenton systems catalyzed by Fh and M-Fh could be caused by two factors: (1) the energy barrier of RDS at $OVs_{(Fe-Fe)}$ or $OVs_{(-Fe)}$ and (2) the oxidation potential of Fh and M-Fh. Clearly, both factors are favorable for the generation of HO· for 5 %Cu-Fh, leading to the highest HO· concentration in this system (137.1 μmol/L). On the other hand, the concentration of HO· (Co-Fh > Fh > Mn-Fh) correlates well with the energy barrier of RDS at $OVs_{(-Fe)}$ in the systemes (Co-Fh < Fh < Mn-Fh), but not with their oxidizing capacity (Co-Fh ≈ Fh ≈ Mn-Fh). As such, it is reasonable to believe that the relative contribution of the two factors in generating HO· is quite different for these catalysts, which further resulted in the concentration difference of HO· in these systems.

The decomposition efficiency of H_2O_2 in Fh and 5 %M-Fh heterogeneous Fenton systems was measured as well in this work. The decomposition of H_2O_2 follows the order: 5 %Co-Fh ≈ 5 %Cu-Fh > 5 % Mn-Fh > Fh (Fig. 3d), and the decomposition kinetics were fitted with the pseudo-first-order equation, with the calculated K_{app} being 0.069, 0.066, 0.046, 0.033 min^{-1}, respectively (Fig. 3e). Considering the

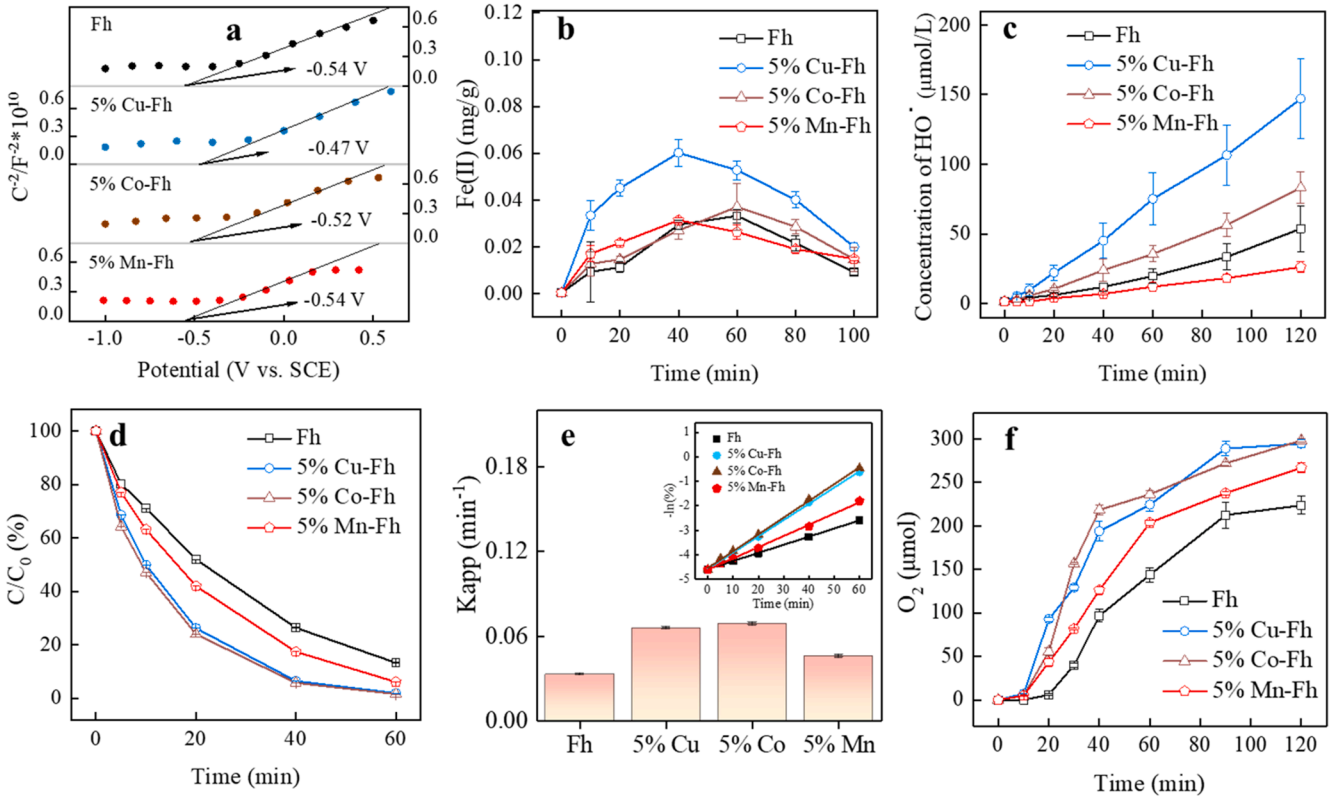

Fig. 3. (a) Mott-Schottky plots of Fh and 5 %M-Fh collected at a frequency of 2 kHz; (b) concentration of generated Fe(II) on catalysts in the heterogeneous Fenton reaction; (c) concentration of HO· in the heterogeneous Fenton reaction; (d) H_2O_2 consumption in the heterogeneous Fenton reaction; (e) apparent H_2O_2 decomposition rate constants of Fh and 5 %M-Fh; (f) O_2 production in the heterogeneous Fenton reaction. [Catalyst dosage] = 1.0 g L^{-1}; [BPA] = 10.0 mg/L; [H_2O_2] = 10.0 mmol L^{-1}; pH = 3.

inconsistence of H_2O_2 decomposition and $HO^{\cdot}$ generation in these systems (e.g., high H_2O_2 decomposition while low $HO^{\cdot}$ generation in 5 % Mn-Fh), we propose that part of the added H_2O_2 were decomposed into O_2 through the following reactions [48,58].

$$HO_2^- + HO_2^- \rightarrow H_2O_2 + O_2 \quad (4)$$

$$\equiv Fe(III) + HO_2^- \rightarrow \equiv Fe(II) + O_2 + H^+ \quad (5)$$

$$\equiv Fe(III) + O_2^{\cdot-} \rightarrow \equiv Fe(II) + O_2 \quad (6)$$

$$HO_2^- + H_2O_2 \rightarrow H_2O + O_2 + HO^{\cdot} \quad (7)$$

$$HO_2^- + HO^{\cdot} \rightarrow H_2O + O_2 \quad (8)$$

As such, the production of O_2 in these systems was quantified, and the obtained values follow the the order 5 %Co-Fh ≈ 5 %Cu-Fh > 5 % Mn-Fh > Fh (Fig. 3f), consistent with the trend of H_2O_2 decomposition. Besides, the detected O_2 concentration is larger than the $HO^{\cdot}$ concentration in these systems (Fig. 3c and 3f), which explains the consistence of H_2O_2 decomposition with O_2 generation but inconsistence with $HO^{\cdot}$ generation.

3.5. Heterogeneous Fenton catalytic activities

The experiments involving BPA degradation were carried out to validate the heterogeneous Fenton catalytic activities of Fh and M-Fh (with the doping content of 1 % or 5 %). All samples show a weak adsorption capacity toward BPA within 30 min (Fig. 4a and b). The evident degradation of BPA is observed by all samples when H_2O_2 was added, with the degradation efficiency decreasing in the order: Cu-Fh > Fh > Co-Fh > Mn-Fh (Fig. 4a and b).

The degradation kinetics of BPA over Fh and M-Fh were fitted with the pseudo-first-order equation to directly compare the heterogeneous Fenton catalytic activities (Fig. 4c and d). These results further confirm that metal-doping can change the Fenton activity of Fh, and it becomes more obvious with the increment of doping content of metal cations. In specific, the apparent rate constant (K_{app}) in the 5 %Cu-Fh system is 0.0074 min^{-1}, much larger than those in the pure Fh system (0.0048 min^{-1}) and 1 %Cu-Fh system (0.0052 min^{-1}). Conversely, the calculated K_{app} in the 5 %Co-Fh (0.0018 min^{-1}) and 5 %Mn-Fh (0.0008 min^{-1}) system is much smaller than those in the Fh system and in the systems with less doped ions (the calculated K_{app} in the 1 %Co-Fh and 1 %Mn-Fh is 0.004 min^{-1} and 0.003 min^{-1}).

The dominant reactive ROS species for the degradation of BPA were further detected, and 5 %M-Fh were selected as representatives (Fig. 4e). When 5 mM of IPA (i.e., the scavenger of $HO^{\cdot}$) was added, the removal rate of BPA is inhibited by 70 %, 69 %, 74 %, and 79 % in the Fh, 5 %Cu-Fh, 5 %Co-Fh, and 5 %Mn-Fh systems, respectively, after 120 min's reaction. These results indicate that $HO^{\cdot}$ plays a dominant role in BPA degradation, well consistent with previous studies [55,56]. In addition, the EPR signal of $O_2^{\cdot-}$ is observed in all reaction systems after the addition of H_2O_2 (Fig. 4f). Above results verify that both $HO^{\cdot}$ and $O_2^{\cdot-}$ are generated in the heterogeneous Fenton process, according to the reactions shown in Eq. 2 and Eq. (1), respectively.

3.6. The underlying mechanisms for BPA degradation through Fenton reaction in the M-Fh systems

Above results well show that doping transition metals in Fh can affect the structure of Fh, and thus the activation of H_2O_2 and the Fenton reactivity as well. According to above discussion, the underlying reaction mechanisms for BPA degradation through Fenton reaction in the M-Fh systems were proposed (Scheme 1). Firstly, the doping of metal ions can create new OVs to stimulate the generation of $HO^{\cdot}$ with different energy barriers (reaction I in Scheme 1). Secondly, doping metal ions will influence the oxidation potential of Fh, and thereby affect the Fe (II)/Fe(III) redox cycle (reaction II in Scheme 1). The synergistic effect of

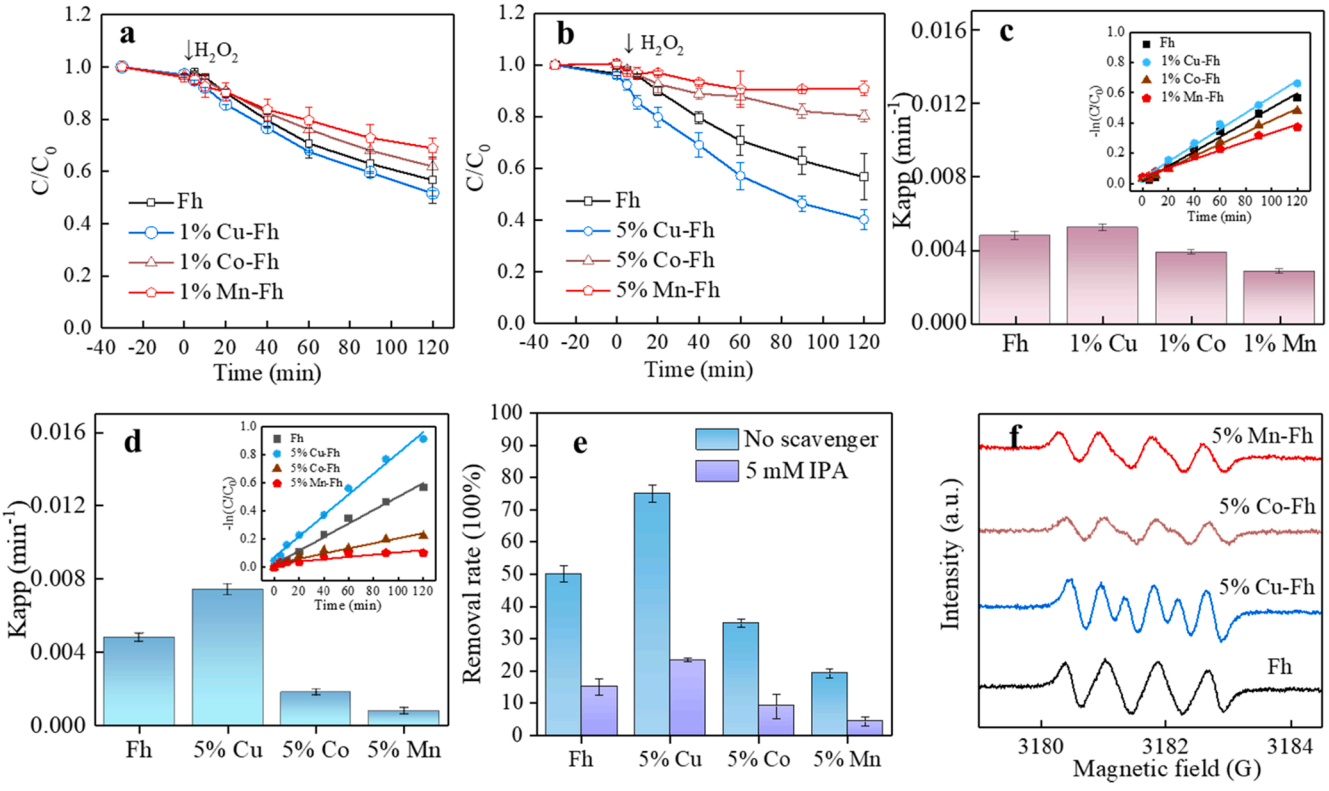

Fig. 4. (a) Degradation kinetics of BPA catalyzed by Fh and 1 %M-Fh; (b) degradation kinetics of BPA catalyzed by Fh and 5 %M-Fh; (c) apparent degradation rate constants of Fh and 1 %M-Fh; (d) apparent degradation rate constants of Fh and 5 %M-Fh; (e) the removal rate of BPA in the systems with or without the addition of IPA; (f) the EPR spectra of DMPO-O_2 adducts produced by Fh and 5 %M-Fh. [Catalyst dosage] = 1.0 g L^{-1}; [BPA] = 10.0 mg/L; [H_2O_2] = 10.0 mmol L^{-1}; pH = 3.

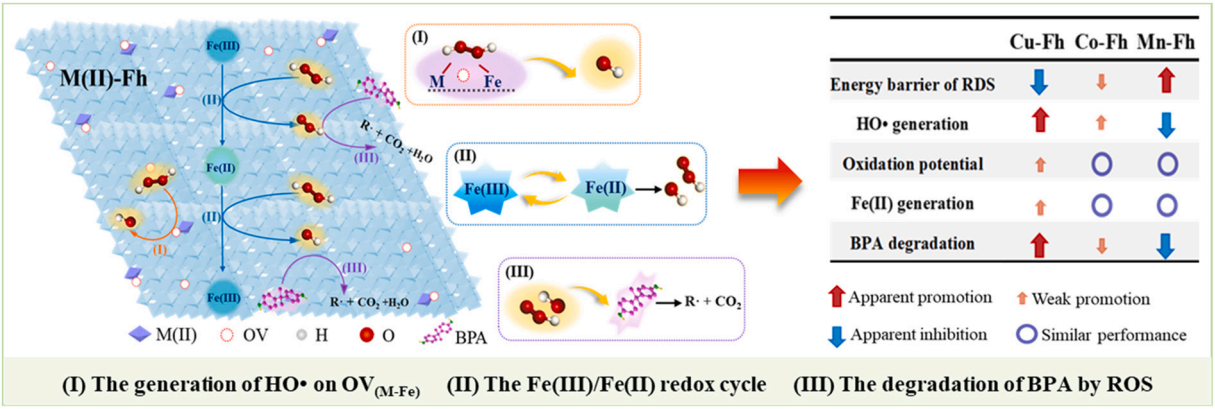

Scheme 1. The underlying reaction mechanisms for BPA degradation during Fenton reaction in the M-Fh systems.

these two aspects determine the efficient catalyzing of H_2O_2 into $HO^{\cdot}$, and thus the degradation of BPA (reaction III in Scheme 1).

In particular, 5 %Cu-Fh is the most efficient catalyst among the studied samples and shows high efficiency in decomposing H_2O_2 into $HO^{\cdot}$ and thus degrading BPA. The superior performance of 5 %Cu-Fh can be attributed to the lowest energy barrier to generate $HO^{\cdot}$ at $OVs_{(Cu\text{-}Fe)}$ and the highest oxidation capacity for accepting electrons from H_2O_2 to reduce Fe(III). Therefore, the concentrations of both $HO^{\cdot}$ and Fe(II) in the 5 %Cu-Fh system are the highest.

On the other hand, the 5 %Co-Fh and 5 %Mn-Fh systems decreased the degradation of BPA. The oxidation potential of 5 %Co-Fh and 5 % Mn-Fh is close to that of Fh, and therefore the generation of Fe(II) on these samples should be comparable. However, the generation of $HO^{\cdot}$ in the 5 %Co-Fh and 5 %Mn-Fh systems is not remarkably influenced by the oxidation potential, but is highly dependent on the energy barrier of $HO^{\cdot}$ generation at $OVs_{(Co\text{-}Fe)}$ and $OVs_{(Mn\text{-}Fe)}$. Therefore, the concentration of $HO^{\cdot}$ in the Fh, 5 %Co-Fh and 5 %Mn-Fh systems follows the order 5 %Co-Fh > Fh > 5 %Mn-Fh, consistent with the trend of energy barrier of $HO^{\cdot}$ generation at $OVs_{(^{-}Fe)}$.

A number of previous studies have concerned the Fenton activity of other metal-doped iron (oxyhydr)oxides (e.g., magnetite, goethite, and hematite), and different mechanisms were proposed to explain the change of activity resulting from doping [51,59–61]. One well recognized reason is the variation of adsorption capacity toward organic contaminants, which is attributed to the change of specific surface area and surface groups after doping metals [9]. However, both Fh and M-Fh show a weak adsorption capacity toward BPA due to the lack of strong interaction affinity towards BPA [12,13], and thus the adsorption capacity of Fh/M-Fh should not be an important factor controlling the degradation of BPA in this work.

Several studies also proposed that the doped metals may affect the cycling rate of Fe(II)/Fe(III) on the catalysts [33,34,51]. Specifically, the redox pairs of transition metals (e.g., Cu(I)/Cu(II), Co(II)/Co(III), and Mn(II)/Mn(III)) may participate in the redox cycling of Fe(II)/Fe(III) to change the electron transfer process [33,34,51]. However, detecting the electron transfer between these metals is not easy, and our results also show that the Fe(II) contents on Fh, Mn-Fh, and Co-Fh are indeed comparable (Fig. 3c). Besides, the electric potential of metal ions in an aqueous solution might not suit the reactions on solid phase after doping, as their electric potential in the crystal structure of minerals will be quite different [62]. As such, instead of just focusing on redox pairs of the doped metals, we analyzed the electronic structure of the whole resulting catalysts, and combined it with the detected solid Fe(II) contents to directly compare the capability of the catalysts in accepting electrons from H_2O_2 to reduce Fe(III).

The influences of OVs created by doped metal ions in iron (oxyhydr) oxides (i.e., $OV_{M\text{-}Fe}$) in decomposing H_2O_2 into $HO^{\cdot}$ was already verified by previous experimental studies [53,63,64]. For instance, Jin et al. reported that the Cu-doped Fe_3O_4@FeOOH showed a higher $HO^{\cdot}$ content than Fe_3O_4@FeOOH, and the authors proposed that the generated OVs on the doped sample helped the decomposition of H_2O_2 into $HO^{\cdot}$ [48]. On the other hand, some studies performed DFT calculations and claimed that OVs may decompose H_2O_2 to form an H_2O molecule and an adsorbed O, and then the adsorbed O will desorb as O_2. However, few experiments have directly demonstrated the formation of O_2 on the OVs. The energy of heterogeneous H_2O_2 dissociation on $OV_{(Fe\text{-}Fe)}$ is -1.70 eV in this work (Fig. S3), which is smaller than the dissociation of H_2O_2 into two hydroxyl groups (-0.90 eV). From the energetic aspect, the heterogeneous dissociation of H_2O_2 on the OVs is an energetically more favourable process. However, from the aspect of the H_2O_2 dissociation process on OVs, homogeneous dissociation (i.e., the cleavage of O—O bond) is more straightforward than heterogeneous dissociation. The steps of heterogeneous H_2O_2 dissociation require the breaking of at least two bonds (i.e., the cleavage of O—H bond and O—O bond) and the recombination of newly formed atoms [65,66]. In particular, the recombination of newly formed atoms to form water is limited by the probability of atomic collision [67]. Overall, the homogeneous and heterogeneous dissociation of H_2O_2 has advantages in the above two aspects, respectively, and both two ways are possible in this work. However, we did not discuss the heterogeneous dissociation of H_2O_2 on the OVs because this work focuses on the effect of doping metals on the heterogeneous Fenton activity, in which $HO^{\cdot}$ plays a dominant role in BPA degradation and the oxidizing capacity of $HO^{\cdot}$ is much higher than that of O_2 [59]. Therefore, this work just focused on the dissociation of H_2O_2 into two hydroxyl groups (i.e., homogeneous dissociation) rather than the heterogeneous dissociation of H_2O_2 into water and adsorbed O (i.e., heterogeneous dissociation). In addition, understanding the effects of $OVs_{(^{-}Fe)}$ on H_2O_2 decomposition and $HO^{\cdot}$ generation behaviors at the atomic scale is still a challenge. On the other hand, DFT calculations can provide accurate descriptions of atomic structures and electronic properties to explore the underlying mechanisms of generating $HO^{\cdot}$ at OVs. [35,47]. In this work, we clarified the detailed reaction process for $OV_{(^{-}Fe)}$, inducing the adsorption and the heterolytic dissociation of H_2O_2 into an adsorbed OH^{-} and a free $HO^{\cdot}$ through DFT calculations. Moreover, we calculated the energy of each reaction step on $OV_{(^{-}Fe)}$ and then found the energy barrier of $HO^{\cdot}$ generation at $OV_{(^{-}Fe)}$ is quite different for Fh and M-Fh catalysts, which further resulted in the concentration difference of $HO^{\cdot}$ in these systems.

4. Conclusion

This work presents a comprehensive study of the structure and Fenton reactivity of transition metal doped Fh. The obtained results clarified how the different doped metals influence the activation of H_2O_2 through the energy barrier of $HO^{\cdot}$ generation at $OV_{(^{-}Fe)}$ and the oxidation potential of the M-Fh. In particular, Cu-Fh is the most efficient

catalyst and shows high efficiency in activating H_2O_2 into $HO^{\cdot}$, owing to its lowest energy barrier for generating $HO^{\cdot}$ at OVs and the highest oxidation capacity for reducing Fe(III) to Fe(II). However, with an inapparent change of oxidation capacity for Co-Fh and Mn-Fh (compared with Fh), the generation of $HO^{\cdot}$ in these systems is highly dependent on the energy barrier difference of $HO^{\cdot}$ generation at $OV_{(^{-}Fe)}$. As such, the concentrations of $HO^{\cdot}$ in the Fh, Co-Fh, and Mn-Fh systems follow the same trend as the energy barrier (i.e., Co-Fh > Fh > Mn-Fh). With the combination of above factors, the overall Fenton activity of the samples in decomposing bisphenol A decreases in the order Cu-Fh > Fh > Co-Fh > Mn-Fh. The proposed structural and electronic effects in this work provide novel information for the understanding of the Fenton activity of doped Fh and can help the design of Fh-based novel heterogeneous Fenton catalysts as well.

CRediT authorship contribution statement

Qingru Xie: Methodology, Investigation, Formal analysis, Visualization, Writing – original draft. **Yanping Zhu:** Methodology, Writing – review & editing, Validation. **Haiyang Xian:** Formal analysis. **Qingze Chen:** Formal analysis. **Chengshuai Liu:** Methodology. **Fei Wu:** Methodology. **Xiaoliang Liang:** Methodology. **Runliang Zhu:** Conceptualization, Validation, Investigation, Resources, Writing – review & editing, Supervision, Funding acquisition, Project administration.

Declaration of Competing Interest

The authors declare that they have no known competing financial interests or personal relationships that could have appeared to influence the work reported in this paper.

Data availability

Data will be made available on request.

Acknowledgments

The authors would like to thank Haoyang Fu at the University of Tongji for his assistance with DFT calculation. This work was financially supported by the National Natural Science Foundation of China (No. 41872044, No.42207069), National Science Fund for Distinguished Young Scholars (No. 42225203, International Partnership Programme of the International Cooperation Bureau, Chinese Academy of Sciences (132744KYSB20200001_o), and Science and Technology Planning Project of Guangdong Province, China (2020B1212060055)..

Appendix A. Supplementary material

Supplementary data to this article can be found online at https://doi.org/10.1016/j.apsusc.2023.156913.

References

[1] Y.X. Cao, X.Z. Yuan, Y.L. Zhao, H. Wang, In-situ soil remediation via heterogeneous iron-based catalysts activated persulfate process: A review, Chem. Eng. J. 431 (2022), 133833, https://doi.org/10.1016/j.cej.2021.133833.
[2] A.V. Karim, Y.L. Jiao, M.H. Zhou, P.V. Nidheesh, Iron-based persulfate activation process for environmental decontamination in water and soil, Chemosphere 265 (2021), 129057, https://doi.org/10.1016/j.chemosphere.2020.129057.
[3] L. Marcon, J. Oliveras, V.F. Puntes, In situ nanoremediation of soils and groundwaters from the nanoparticle's standpoint: A review, Sci. Total. Environ. 791 (2021), 148324, https://doi.org/10.1016/j.scitotenv.2021.148324.
[4] G.H. Yu, Y. Kuzyakov, Fenton chemistry and reactive oxygen species in soil: Abiotic mechanisms of biotic processes, controls and consequences for carbon and nutrient cycling, Earth-Sci. Rev. 214 (2021), 203525, https://doi.org/10.1016/j.earscirev.2021.103525.
[5] Z.Y. Xiang, H. Wang, R.Z. Wen, Y.M. Li, J.H. Yang, J.L. Yin, J. Wang, W.L. Wang, Incorporating Se vacancies into $FeSe_2/Fe_2O_3$@C to enhance H_2O_2 adsorption for efficient photo-Fenton removal of As(III), Appl. Surf. Sci. 606 (2022), 154879, https://doi.org/10.1016/j.apsusc.2022.154879.
[6] P.V. Nidheesh, Heterogeneous Fenton catalysts for the abatement of organic pollutants from aqueous solution: a review, RSC. Adv. 5 (2015) 40552, https://doi.org/10.1039/C5RA02023A.
[7] Z. Chen, C. Lian, K. Huang, J.H. Jia, Q.Y. Yan, J.L. Zhang, M.Y. Xing, "Small amount for multiple times" of H_2O_2 feeding way in MoS_2-Fe_x heterogeneous fenton for enhancing sulfadiazine degradation, Chinese Chem. Lett. 33 (2022) 1365–1372, https://doi.org/10.1016/j.cclet.2021.08.016.
[8] M.F. Dapaah, Q.J. Niu, Y.Y. Yu, T.Y. You, B.J. Liu, L. Cheng, Efficient persistent organic pollutant removal in water using MIL-metal-organic framework driven Fenton-like reactions: A critical review, Chem. Eng. J. 431 (2022), 134182, https://doi.org/10.1016/j.cej.2021.134182.
[9] X.L. Liang, Y.H. Zhong, S.Y. Zhu, L.Y. Ma, P. Yuan, J.X. Zhu, H.P. He, Z. Jiang, The contribution of vanadium and titanium on improving methylene blue Decolorization through heterogeneous UV-Fenton reaction catalyzed by their co-doped magnetite, J. Hazard. Mater. 199–200 (2012) 247–254, https://doi.org/10.1016/j.jhazmat.2011.11.007/.
[10] W.Y. Gu, X.Y. Huang, Y.H. Tian, M. Cao, l. Zhou, Y. Zhou, J. Lu, J.Y. Lei, Y.B. Zhou, L.Z. Wang, Y.D. Liu, J.L. Zhang, High-efficiency adsorption of tetracycline by cooperation of carbon and iron in a magnetic Fe/porous carbon hybrid with effective Fenton regeneration, Appl. Surf. Sci. 538 (2021), 147813, https://doi.org/10.1016/j.apsusc.2020.147813.
[11] T.Y. Xu, R.L. Zhu, H. Shang, Y.B. Xia, X. Liu, L.Z. Zhang, Photochemical behavior of ferrihydrite-oxalate system: Interfacial reaction mechanism and charge transfer process, Water. Res. 159 (2019) 10–19, https://doi.org/10.1016/j.watres.2019.04.055.
[12] T.Y. Xu, R.L. Zhu, G.Q. Zhu, J.X. Zhu, X.L. Liang, Y.P. Zhu, H.P. He, Mechanisms for the enhanced photo-Fenton activity of ferrihydrite modified with $BiVO_4$ at neutral pH, Appl. Catal. B Environ. 212 (2017) 50–58, https://doi.org/10.1016/j.apcatb.2017.04.064.
[13] Y.P. Zhu, R.L. Zhu, H. Yan, Y. Fu, H. Xi, G. Zhou, J. Zhu, H. He Zhu, Visible-light Ag/AgBr/ferrihydrite catalyst with enhanced heterogeneous photo-Fenton reactivity via electron transfer from Ag/AgBr to ferrihydrite, Appl. Catal. B Environ. 239 (2018) 280–289, https://doi.org/10.1016/j.apcatb.2018.08.025.
[14] R.L. Zhu, Y.P. Zhu, H.Y. Xian, L.X. Yan, H.Y. Fu, G.Q. Zhu, Y.F. Xi, J.X. Zhu, H. P. He, CNTs/ferrihydrite as a highly efficient heterogeneous Fenton catalyst for the degradation of bisphenol A: The important role of CNTs in accelerating Fe(III)/Fe(II) cycling, Appl. Catal. B Environ. 270 (2020) 1–10, https://doi.org/10.1016/j.apcatb.2020.118891.
[15] B. Thamdrup, Bacterial Manganese and Iron Reduction in Aquatic Sediment, Adv. Microb. Ecol. 16 (2000) 41–82, https://doi.org/10.1007/978-1-4615-4187-5_2.
[16] S. Hiemstra, Surface and mineral structure of ferrihydrite, Geochim. Cosmochim. Acta. 105 (2013) 316–325, https://doi.org/10.1016/j.gca.2012.12.002.
[17] F.M. Michel, L. Ehm, S.M. Antao, P.L. Lee, P.J. Chupas, G. Liu, D.R. Strongin, M. A. Schoonen, B.L. Phillips, J.B. Parise, The structure of ferrihydrite, a nanocrystalline material, Science 316 (5832) (2007) 1726–1729, https://doi.org/10.1126/science.1142525.
[18] A.C. Cismasu, F.M. Michel, J.F. Stebbins, C. Levard, G.e. Brown Jr, Properties of impurity-bearing ferrihydrite I. Effects of Al content and precipitation rate on the structure of 2-line ferrihydrite, Geochim. Cosmochim. Acta. 92 (2012) 275–291, https://doi.org/10.1016/j.gca.2012.06.010.
[19] A.C. Cismasu, C. Levard, F.M. Michel, G.E. Brown Jr, Properties of impurity-bearing ferrihydrite II: Insights into the surface structure and composition of pure, Al- and Si-bearing ferrihydrite from Zn(II) sorption experiments and Zn K-edge X-ray absorption spectroscopy, Geochim. Cosmochim. Acta. 119 (2013) 46–60, https://doi.org/10.1016/j.gca.2013.05.040.
[20] L. Zhang, F.L. Fu, G.D. Yu, G.Z. Sun, B. Tang, Fate of Cr(VI) during aging of ferrihydrite-humic acid co-precipitates: Comparative studies of structurally incorporated Al(III) and Mn(II), Sci. Total. Environ. 807 (2022), 151073, https://doi.org/10.1016/j.scitotenv.2021.151073.
[21] R. Giovanoli, R.M. Cornell, Crystallization of Metal Substituted Ferrihydrites, Z. Pflanzenernähr. Bodenkd. 155 (1992) 455–460, https://doi.org/10.1002/jpln.19921550517.
[22] M. Mohapatra, D. Hariprasad, L. Mohapatra, S. Anand, B.K. Mishra, Mg-doped nano ferrihydrite—A new adsorbent for fluoride removal from aqueous solutions, Appl. Surf. Sci. 258 (2012) 4228–4236, https://doi.org/10.1016/j.apsusc.2011.12.047.
[23] H. Liu, F.L. Cao, P. Li, Y. Wei, D.L. Hou, The formation of discoid hematite particles from Al-doped ferrihydrite: The effect of trace Fe(II) and the introduction procedures of Al(III), Chem. Eng. J. 157 (2010) 254–262, https://doi.org/10.1016/j.cej.2009.12.018.
[24] C.W. Liang, F.l. Fu, B. Tang, Mn-incorporated ferrihydrite for Cr(VI) immobilization: Adsorption behavior and the fate of Cr(VI) during aging, J. Hazard. Mater. 417 (2021), 126073, https://doi.org/10.1016/j.jhazmat.2021.126073.
[25] C.Y. Ni, S. Liu, L.J. Cui, Z. Han, L. Wang, R.F. Chen, H. Liu, Adsorption performance of Cr(VI) onto Al-free and Al-substituted ferrihydrites, RSC Adv. 6 (2016) 66412, https://doi.org/10.1039/C6RA09465A.
[26] W. Buda, B. Czech, Preparation and characterization of C, N-codoped TiO_2 photocatalyst for the degradation of diclofenac from wastewater, Water, Sci. Technol. 68 (2013) 1322–1328, https://doi.org/10.2166/wst.2013.369.
[27] H.Y. Fu, R.Z. Wang, Q.Y. Xu, M.W. Laipan, C.L. Tang, W.X. Zhang, L. Ling, Facile construction of Fe/Pd-doped graphite carbon nitride for effective removal of doxorubicin: Performance, mechanism and degradation pathways, Appl. Catal. B Environ. 299 (2021), 120686, https://doi.org/10.1016/j.apcatb.2021.120686.
[28] J.M. Li, X.D. Pei, Z.Z. Wang, Y. Li, G.K. Zhang, Boosted charge transfer and selective photocatalytic CO_2 reduction to CH_4 over sulfur-doped $K_{0.475}WO_3$

nanorods under visible light: Performance and mechanism insight, Appl. Surf. Sci. 605 (2022), 154632, https://doi.org/10.1016/j.apsusc.2022.154632.
[29] W.J. Dai, Y. Chen, X. Liu, H.G. Xiang, C. Xu, G. Zheng, G. Chen, Optimal doping elements for inhibiting surface-diffusion of adatoms on Cu_3Sn, Appl. Surf. Sci. 609 (2023), 155003, https://doi.org/10.1016/j.apsusc.2022.155003.
[30] J. Ren, L.S. Jiang, Y. Li, G.K. Zhang, Cobalt doped bismuth oxysulfide with abundant oxygen vacancies towards tetracycline degradation through peroxymonosulfate activation, Sep. Purif. Technol. 275 (2021), 119100, https://doi.org/10.1016/j.seppur.2021.119100.
[31] J. Wang, L. Ling, Z.L. Deng, W.X. Zhang, Nitrogen-doped iron for selective catalytic reduction of nitrate to dinitrogen, Sci. Bull. 65 (2020) 926–933, https://doi.org/10.1016/j.scib.2020.02.015.
[32] I.R. Guimaraes, A. Giroto, L.C. Oliveira, M.C. Guerreiro, D.Q. Lima, J.D. Fabris, Synthesis and thermal treatment of cu-doped goethite: oxidation of quinoline through heterogeneous Fenton process, Appl. Catal. B Environ. 91 (2009) 581–586, https://doi.org/10.1016/j.apcatb.2009.06.030.
[33] S.R. Pouran, A.A.A. Raman, W.M.A.W. Daud, Review on the application of modified iron oxides as heterogeneous catalysts in Fenton reactions, J. Cleaner Prod. 64 (2014) 24–35, https://doi.org/10.1016/j.jclepro.2013.09.013.
[34] J. Xu, Y. Li, B. Yuan, C. Shen, M. Fu, H. Cui, W. Sun, Large scale preparation of Cu-doped α-FeOOH nanoflowers and their photo-Fenton-like catalytic degradation of diclofenac sodium, Chem. Eng. J. 291 (2016) 174–183, https://doi.org/10.1016/j.cej.2016.01.059.
[35] J. Jia, P. Zhang, L. Chen, Catalytic decomposition of gaseous ozone over manganese dioxides with different crystal structures, Appl. Catal. B Environ. 189 (2016) 210–218, https://doi.org/10.1016/j.apcatb.2016.02.055.
[36] H. Li, J. Shang, Z.P. Yang, W.J. Shen, Z.H. Ai, L.Z. Zhang, Oxygen Vacancy Associated Surface Fenton Chemistry: Surface Structure Dependent Hydroxyl Radicals Generation and Substrate Dependent Reactivity, Environ. Sci. Technol. 51 (10) (2017) 5685–5694, https://doi.org/10.1021/acs.est.7b00040.
[37] G.X. Zhuang, Y.W. Chen, Z.Y. Zhuang, Y. Yan, J.G. Yu, Oxygen vacancies in metal oxides: recent progress towards advanced catalyst design, Sci. China Mater. 63 (2020) 2089–2118, https://doi.org/10.1007/s40843-020-1305-6.
[38] Y. Xu, M.A.A. Schoonen, The absolute energy positions of conduction and valence bands of selected semiconducting minerals, Am. Mineral. 85 (2000) 543–556, https://doi.org/10.2138/am-2000-0416.
[39] X.B. Chen, S.H. Shen, L.J. Guo, S.S. Mao, Semiconductor-based Photocatalytic Hydrogen Generation, Chem. Rev. 110 (2010) 6503–6570, https://doi.org/10.1021/cr1001645.
[40] F. Cinquini, L. Giordano, G. Pacchioni, Cationic and anionic vacancies on the NiO (100) surface: DFT+U and hybrid functional density functional theory calculations, J. Chem. Phys. 127 (2007) 1–8, https://doi.org/10.1063/1.2796154.
[41] A.E. Harvey Jr., J.A. Smart, E.S. Amis, Simultaneous Spectrophotometric Determination of Iron (II) and Total Iron with 1,10-Phenanthroline, Amis Anal. Chem. 27 (1955) 26–29, https://doi.org/10.1021/ac60097a009.
[42] Iron-ores-Determination of acid-soluble ion (II) content-Titrimetric method. National Standard of the People's Republic of China. GB/T 6730.71-2014.
[43] G. Kresse, J. Furthmüller, Efficiency of ab-initio total energy calculations for metals and semiconductors using a plane-wave basis set, Comput. Mater. Sci. 6 (1996) 15–50, https://doi.org/10.1016/0927-0256(96)00008-0.
[44] J. Larrucea, S. Lid, L.C. Ciacchi, Parametrization of a classical force field for iron oxyhydroxide/water interfaces based on Density Functional Theory calculations, Comp. Mater. Sci. 92 (2014) 343–352, https://doi.org/10.1016/j.commatsci.2014.05.056.
[45] B. Li, H. Metiu, DFT studies of oxygen vacancies on undoped and doped La_2O_3 surfaces, J. Phys. Chem. C. 114 (2010) 12234–12244, https://doi.org/10.1021/jp103604b.
[46] V. Agarwal, H. Metiu, Oxygen vacancy formation on α-MoO_3 slabs and ribbons, J. Phys. Chem. C. 120 (2016) 19252–19264, https://doi.org/10.1021/acs.jpcc.6b06589.
[47] L. Jiao, J.B. Wu, H. Zhong, Y. Zhang, W.Q. Xu, Y. Wu, Y.F. Chen, H.Y. Yan, Q. H. Zhang, W.L. Gu, L. Gu, S.P. Beckman, L. Huang, C.Z. Zhu, Densely Isolated FeN_4 Sites for Peroxidase Mimicking, ACS Catal. 10 (2020) 6422–6429.
[48] H. Jin, X.K. Tian, Y.L. Nie, Z.X. Zhou, C. Yang, Y. Li, L.Q. Lu, Oxygen Vacancy Promoted Heterogeneous Fentonlike Degradation of Ofloxacin at pH 3.2-9.0 by Cu Substituted Magnetic Fe_3O_4@FeOOH Nanocomposite, Environ. Sci. Technol. 51 (2017) 12699–12706, https://doi.org/10.1021/acs.est.7b04503.
[49] C.A. Gorski, M.M. Scherer, Determination of nanoparticulate magnetite stoichiometry by Mossbauer spectroscopy, acidic dissolution, and powder X-ray diffraction: a critical review, Am. Mineral. 95 (2010) 1017–1026, https://doi.org/10.2138/am.2010.3435.
[50] C.M. Chen, C. Meile, J. Wilmoth, D. Barcellos, A. Thompson, Influence of pO_2 on iron redox cycling and anaerobic organic carbon mineralization in a humid tropical forest soil, Environ. Sci. Technol. 52 (2018) 7709–7719, https://doi.org/10.1021/acs.est.8b01368.
[51] Y. Li, G.L. Wei, C.H. Zhang, X.L. Liang, W. Chu, H.P. He, J.W. Stucki, L.Y. Ma, X. J. Lin, J.X. Zhu, Remarkable effect of Co substitution in magnetite on the reduction removal of Cr(VI) coupled with aqueous Fe(II): Improvement mechanism and Cr fate, Sci. Total. Environ. 656 (2019) 400–408, https://doi.org/10.1016/j.scitotenv.2018.11.344.
[52] Costa, M.D.F.F. Lelis, L.C.A. Oliveira, J.D. Fabris, J.D. Ardisson, R.R.V.A. Rios, C. N. Silva, R.M. Lago, Remarkable effect of Co and Mn on the activity of $Fe_{3-x}M_xO_4$ promoted oxidation of organic contaminants in aqueous medium with H_2O_2, Catal. Commun. 4 (2003) 525–529, https://doi.org/10.1016/j.catcom.2003.08.002.
[53] R.G. Nair, S. Mazumdar, B. Modak, R. Bapat, P. Ayyub, K. Bhattacharyya, The role of surface O-vacancies in the photocatalytic oxidation of Methylene Blue by Zn-doped TiO_2: A Mechanistic approach, J. Photoch. Photobio. A. 345 (2017) 36–53, https://doi.org/10.1016/j.jphotochem.2017.05.016.
[54] C.C. Ling, X.F. Liu, H. Li, X.B. Wang, H.Y. Gu, K. Wei, M.Q. Li, Y.B. Shi, H.J. Ben, G. M. Zhan, C. Liang, W.J. Shen, Y.L. Li, J.C. Zhao, L.Z. Zhang, Atomic-Layered Cu_5 Nanoclusters on FeS_2 with Dual Catalytic Sites for Efficient and Selective H_2O_2 Activation, Angew. Chem. Int. Ed. 61 (2022) 202200670.
[55] J.J. Pignatello, E. Oliveros, A. MacKay, Advanced oxidation processes for organic contaminant destruction based on the fenton reaction and related chemistry, Environ. Sci. Technol. 36 (2006) 1–84, https://doi.org/10.1080/10643380500326564.
[56] E.M.R. Rocha, V.J.P. Vilar, A. Fonseca, I. Saraiva, R.A.R. Boaventura, Landfill leachate treatment by solar-driven AOPs, Sol. Energy. 85 (2011) 46–56, https://doi.org/10.1016/j.solener.2010.11.001.
[57] Y.P. Zhu, Q.R. Xie, R.L. Zhu, Y. Lv, Y.F. Xi, J.X. Zhu, J. Fan, Hydrothermal carbons/ferrihydrite heterogeneous Fenton catalysts with low H_2O_2 consumption and the effect of graphitization degrees, Chemosphere 287 (2022), 131933, https://doi.org/10.1016/j.chemosphere.2021.131933.
[58] A.V. Vorontsov, Advancing Fenton and photo-Fenton water treatment through the catalyst design, J. Hazard. Mater. 372 (2019) 103–112, https://doi.org/10.1016/j.jhazmat.2018.04.033.
[59] R.C. Costa, M.F. Lelis, L.C. Oliveira, J.D. Fabris, J.D. Ardisson, R.R. Rios, C.N. Silva, R.M. Lago, Novel active heterogeneous Fenton system based on $Fe_{3-x}M_xO_4$ (Fe Co, Mn, Ni): the role of M^{2+} species on the reactivity towards H_2O_2 reactions, J. Hazard. Mater. 129 (2006) 171–178, https://doi.org/10.1016/j.jhazmat.2005.08.028.
[60] C.L. Pearce, C.M.B. Henderson, N.D. Telling, R.A.D. Pattrick, J.M. Charnock, V. S. Coker, E. Arenholz, F. Tuna, G. van der Laan, Fe site occupancy in magnetite-ulvöspinel solid solutions: a new approach using X-ray magnetic circular dichroism, Am. Mineral. 95 (2010) 425–439, https://doi.org/10.2138/am.2010.3343.
[61] A.C. Silva, R.M. Cepera, M.C. Pereira, D.Q. Lima, J.D. Fabri, L.C.A. Oliveira, Heterogeneous catalyst based on peroxo-niobium complexes immobilized over iron oxide for organic oxidation in water, Appl. Catal. B Environ. 107 (2011) 237–244, https://doi.org/10.1016/j.apcatb.2011.07.017.
[62] X.L. Wang, S.O. Pehkonen, K.A. Ray, Removal of Aqueous Cr(VI) by a Combination of Photocatalytic Reduction and Coprecipitation, Ind. Eng. Chem. Res. 43 (2004) 1665–1672, https://doi.org/10.1021/ie030580j.
[63] W.M. Xie, F.P. Zhou, X.l. Bi, D.D. Chen, Z.J. Huang, Y.H. Li, S.Y. Sun, J.Y. Liu, Decomposition of Nickel(II)-Ethylenediaminetetraacetic acid by Fenton-Like reaction over oxygen vacancies-based Cu-Doped Fe_3O_4@γ-Al_2O_3 catalyst: A synergy of oxidation and adsorption, Chemosphere 221 (2019) 563–572, https://doi.org/10.1016/j.chemosphere.2019.01.083.
[64] N.Q. Zhang, E.P. Tsang, J.Y. Chen, Z.Q. Fang, D.Y. Zhao, Critical role of oxygen vacancies in heterogeneous Fenton oxidation over ceria-based catalysts, J. Colloid. Interf. Sci. 558 (2020) 163–172, https://doi.org/10.1016/j.jcis.2019.09.079.
[65] A.A. Peyghan, S.P. Laeen, S.A. Aslanzadeh, M. Moradi, Hydrogen peroxide reduction in the oxygen vacancies of ZnO nanotubes, Thin Solid Films 556 (2014) 566–570, https://doi.org/10.1016/j.tsf.2014.01.084.
[66] Z.J. Song, B. Wang, J. Yu, C. Ma, C.S. Zhou, T. Chen, Q.Q. Yan, K. Wang, L.S. Sun, Density functional study on the heterogeneous oxidation of NO over α-Fe_2O_3 catalyst by H_2O_2: Effect of oxygen vacancy, Appl. Surf. Sci. 413 (2017) 292–301, https://doi.org/10.1016/j.apsusc.2017.04.011.
[67] W.P. Hong, Y.D. Jung, Plasma Screening Effects on Atomic Collisional Orientation in Quantum Plasmas, IEEE. T. Plasma. Sci. 42 (2014), https://doi.org/10.1109/TPS.2014.2322591.